

Instrument Science Report WFC3 2016-001

The Updated Calibration Pipeline for WFC3/UVIS: A Reference Guide to calwf3 (version 3.3)

R. E. Ryan Jr., S. Deustua, M. Sosey, J. Anderson, S. M. Baggett, V. Bajaj, M. Bourque,
A. Bowers, T. Dahlen, M. Durbin, C. Gosmeyer, H. Gunning, H. Khandrika
J. Mack, J. MacKenty, C. Martlin, V. Kozhurina-Platais, & E. Sabbi

April 18, 2016

ABSTRACT

We report on the major developments to the calibration pipeline (calwf3 version 3.3) for the UVIS channel of the Wide-Field Camera 3. There are three key additions to the software: (1) independent photometric calibrations for the two CCDs, (2) integration of a pixel-based charge-transfer efficiency correction, and (3) masking of sink pixels by means of a new reference file (SNKCFILE). This report is meant to serve as a Reference Guide summarizing the detailed Instrument Science Reports that describe the 2016 reference files and software. We highlight results demonstrating the efficacy of the new version of the calibration pipeline and offer guidance to users planning observations with the UVIS channel. A corollary report presents a step-by-step “cookbook” for common analysis needs. For the sake of completeness, we also mention two minor changes to the processing of IR scanning-mode data that have been incorporated in the new calwf3 (version 3.3).

Table of Contents

1	Introduction	3
2	Two-Chip Photometry	6
2.1	Flat-Field Corrections	6
2.2	Encircled-Energy Curves	8
2.3	Photometric Zeropoints	11
2.4	New Software and Reference Files	12
3	Charge-Transfer Efficiency Corrections	15
3.1	Current WFC3/UVIS CTE Model	15
3.2	Reasons to OMIT the CTE Corrections	16
4	Sink Pixels	17
5	Validation	21
5.1	Photometry and Astrometry	21
5.2	Color-Magnitude Diagram	21
6	Additional Minor Revisions in calwf3 (version 3.3)	23
6.1	Improved UVIS Dark Calibration	23
6.1.1	CTE-corrected reference files	24
6.1.2	Improved temporal accuracy of hot pixel populations	24
6.1.3	Improved accuracy of dark current measurement	24
6.2	Channel-Select Mechanism	26
6.3	Scanning-Mode for IR Data	26
7	Summary	26
8	Acknowledgments	29
9	References	30

1 Introduction

The Wide-Field Camera 3 (WFC3) is a fourth-generation HST instrument capable of imaging and low-resolution spectroscopy from 0.2–1.6 μm with two separate channels: UVIS and IR. The standard data reduction and calibration system for both channels (`calwf3`, version 3.3) was written and is maintained by STScI¹. Here we discuss several major changes to the processing of the UVIS data, as they represent a significant departure from the original methodology. These changes are included in the version 3.3 of `calwf3` (the `calwf3` version number can be found in the fits header as `CAL_VER`), and any data requested through the Mikulski Archive for Space Telescopes (MAST) after Feb. 23, 2016 will be processed with these new tools (and will include a bevy of new header keywords that we discuss below).

The UVIS device consists of two 2051×4096 CCDs with a pixel scale of $0''.0395 \text{ pix}^{-1}$ (see Figure 1 for a layout of the UVIS instrument). There are two primary motivations for the modifications to `calwf3`:

1. By ~ 2012 the effects of radiation damage on the crystal lattice of the CCDs had become severe enough to cause significant losses in charge-transfer efficiency (CTE), such that very faint sources could lose $\sim 50\%$ of their signal (e.g. Noeske et al. 2012). Although mitigation capabilities were built into the system via postflash and/or charge injection (Gialvalisco 2003), on-orbit data showed that a low-level of postflash was more effective (Anderson et al. 2012); therefore the WFC3 team has stopped supporting charge injection. In 2013, J. Anderson released a stand-alone CTE-correction tool², which has now been incorporated in the `calwf3` pipeline.
2. Additionally, the very different quantum efficiencies of the two CCDs (most strikingly at $\lambda \lesssim 3500 \text{ \AA}$) require independent photometric calibrations, particularly for combining UV observations from the different chips (such as with `AstroDrizzle`).

In addition to these two improvements, the UVIS portion of the new `calwf3` (version 3.3) now proceeds along two parallel tracks, providing two sets of fully calibrated images (with and without CTE correction). In either case, if the `FLUXCORR` and `DQICORR` keywords are set to `PERFORM`, then both photometric flux calibration and sink pixel flagging (discussed in more § 4) are also applied.

This document is meant to serve as an overview of the new software system, and we refer the reader to the individual Instrument Science Reports (ISRs) and other publications for detailed discussions and analysis. In a companion ISR, Bajaj et al. (2016) present a *cookbook* for a host of standard reduction needs (for example, recalibration with the new pixel-based CTE algorithm and older versions of the flat fields and zeropoints).

¹The Science Software Branch (SSB): <http://ssb.stsci.edu>

²The software remains available for download at http://www.stsci.edu/hst/wfc3/tools/cte_tools.

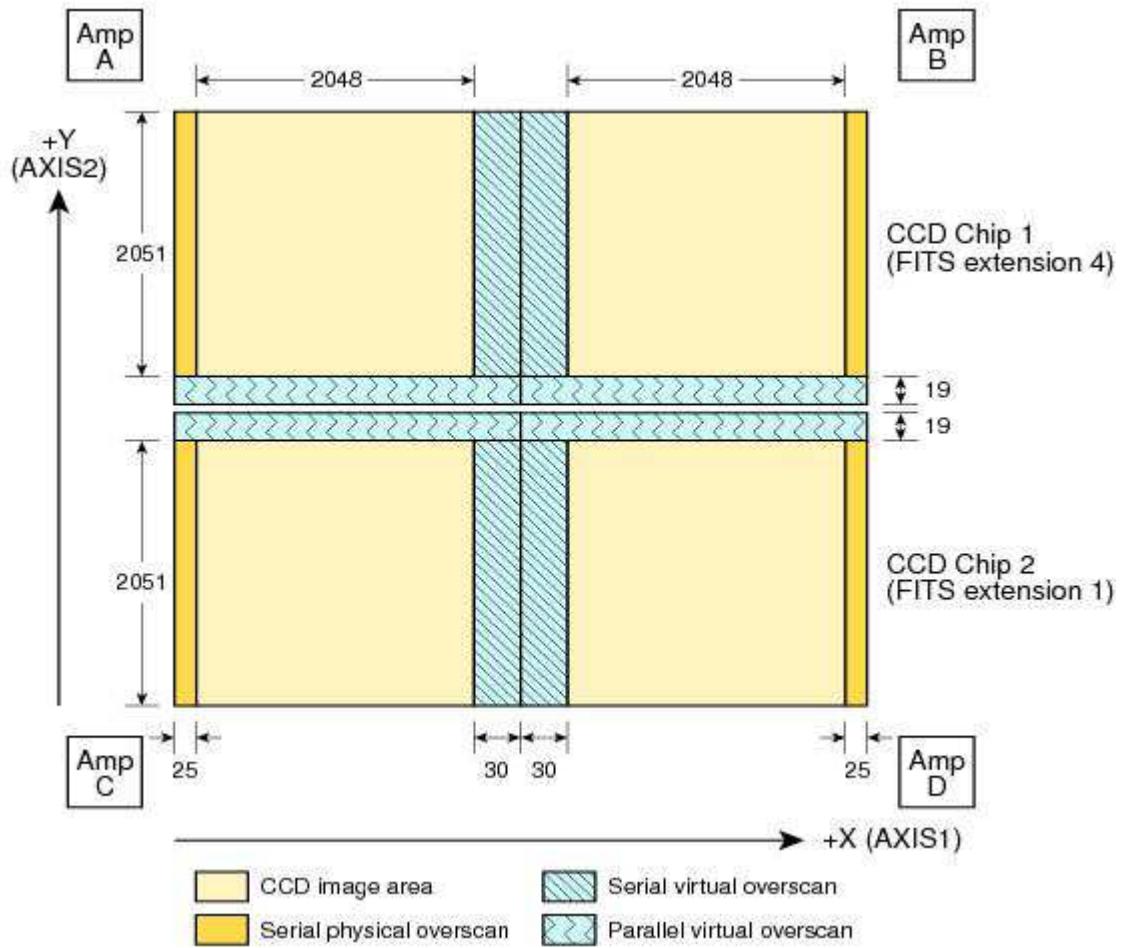


Fig. 1.— The WFC3/UVIS raw full-chip image (graphic taken from Dressel 2015; Figure 6.14). For images throughout this report, we show Chip 1 (UVIS 1) at the top and Chip 2 (UVIS 2) at the bottom.

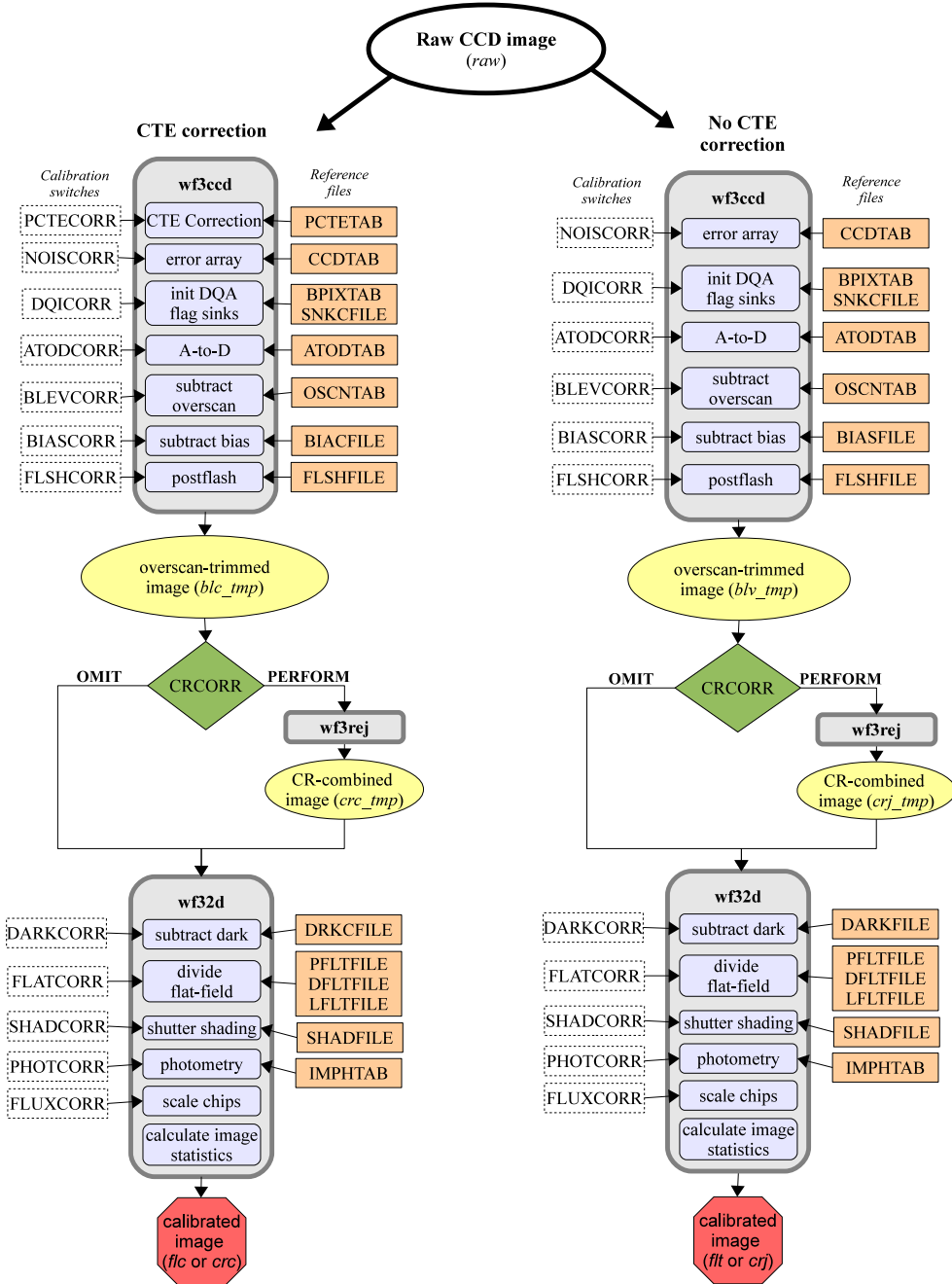


Fig. 2.— Flow chart for `calwf3` (version 3.3) for UVIS. The new UVIS pipeline now proceeds along two parallel tracks for processing the RAW data — one with and one without corrections for charge-transfer efficiency. Here the colors/shapes indicate various components of the pipeline: white/dashed boxes are calibration switches (that can be set to OMIT or PERFORM), light gray areas are large computational modules, light blue boxes indicate individual processes within a module, orange boxes refer to the calibration reference files, yellow ellipses indicate temporary products, and the red octagons represent the end products. Both sets of output products (with and without CTE corrections) then flow into `AstroDrizzle` and DRZ/DRC products are generated. NOTE: The sink pixels are flagged after the `BIASCORR`, but are flagged based on the `DQICORR` setting. This figure was adapted from Figure 2 of Baggett, Anderson, & Sosey (2014).

2 Two-Chip Photometry

The two WFC3/UVIS e2v detectors have very different quantum efficiencies, particularly for $\lambda \lesssim 3500 \text{ \AA}$ (see Figure 3) where UVIS 2 is considerably more sensitive than UVIS 1. This difference motivates photometric calibrations to be independently determined for the two WFC3/UVIS CCDs. New flat fields for all full-frame filters (ie. not the quad filters or the grism) have been created, with low-frequency corrections for in-flight sensitivity separately computed for each chip. The flat fields are *now normalized to the median value of each chip*, removing any correction for sensitivity offsets between chips in the flat-field images. *The zeropoints are now calculated for each chip independently using observations of white-dwarf standards from the calibration program.* Therefore `calwf3` (version 3.3) has been modified to scale the UVIS2 chip data by the ratio of the sensitivity of UVIS1 to UVIS2 so that the source flux in calibrated observations will be the same regardless of whether it was measured in UVIS1 or UVIS2. Full-frame calibrated (FLT/FLC) and drizzled (DRZ/DRC)³ data products will therefore be continuous across the full detector field-of-view, so that users only need to apply a single zeropoint (corresponding to UVIS1) to the full frame image. **While the new solutions represent a significant change in the calibration software and reference files, this change should be invisible to users performing UVIS photometry as discussed below.**

2.1 Flat-Field Corrections

The creation of the new chip-dependent flat fields is described by Mack (2016). In summary, the new flat-field images are based on the 2009-ground flats, corrected for a large-scale internal reflection or *flare* using a geometric model of the light path. Low-frequency differences in the in-flight detector response (L-flats) were derived for both chips from dithered observations of stars in ω Centauri for 10 broadband filters that cover the full UVIS wavelength range. For the remaining 32 UVIS filters, the combined correction (including both the flare and the L-flat) was computed by interpolation based on the pivot wavelengths. These new flat fields have three key differences with respect to the December 2011 flat fields (Mack et al. 2013), which have been used prior to the release of the `calwf3` (version 3.3).

1. The L-flats are now computed from CTE-corrected images.
2. The L-flats are computed from photometry of stars dithered for each chip.
3. Instead of normalizing both chips to a small region on amp A, the flats are now independently normalized by the median value of good pixels for each chip. This removes any sensitivity

³As a general rule, images corrected for losses in charge-transfer efficiency will have the last letter in their three-letter acronym changed into a 'c'. For example, an FLT file will become an FLC.

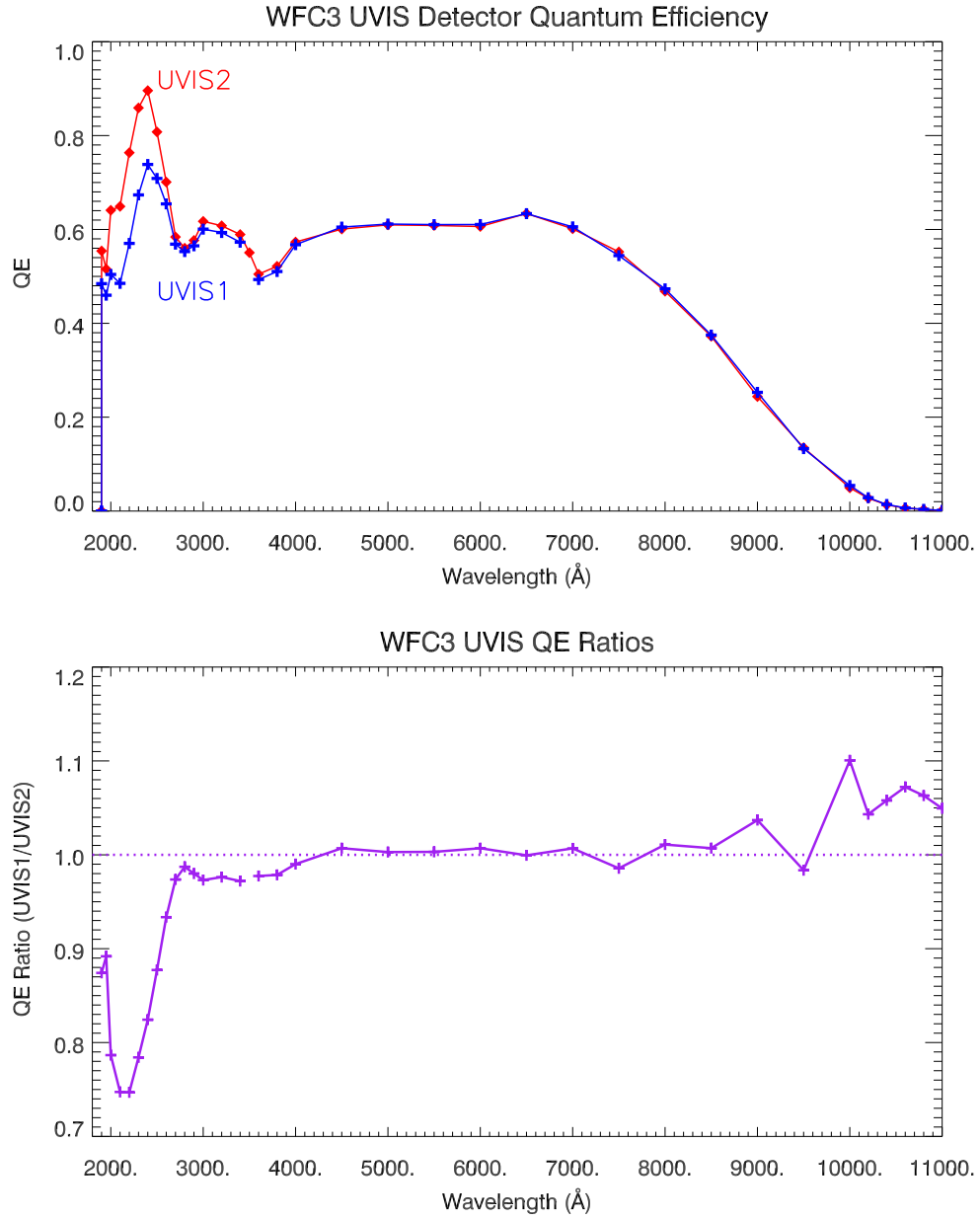


Fig. 3.— Quantum efficiencies for the UVIS CCDs. These data were derived from ground-based observations, and at $\lambda \lesssim 3500$ Å highlight the need for the chip-dependent calibrations.

offsets in the flats, and relies on the zeropoint calibration data to determine the chip sensitivity ratio with wavelength (see Figures 4 and 5).

For the four bluest filters (F218W, F225W, F275W, F280N), the flat fields include an additional correction to the chip sensitivities to account for the variable operating temperature of the detector. These four flats were obtained in ambient conditions ($-42\text{ }^{\circ}\text{C}$) during ground testing and were corrected with in-flight data (obtained at $-82\text{ }^{\circ}\text{C}$). Calibration observations of white-dwarf standard stars stepped across two UVIS chips indicate large photometric variations with position (variations of order a few percent). These residual pixels directly correlate with a crosshatch pattern in the flat fields, which corresponds to a detection-layer structure in the CCDs at spatial scales of $\sim 50 - 100$ pixels and varies with temperature. Photometric residuals of standard-star data processed with these new UV flat fields are now reduced from $\sim 7\%$ to $\sim 3\%$ (peak-to-peak). Mack et al. (2016) describe the corrections for this mid-frequency structure that has been incorporated into these new flat fields.

2.2 Encircled-Energy Curves

The UVIS encircled energy curves were derived from calibration observations from three HST white-dwarf standards (GD71, GD153, GD191B2B) taken in all 42 full-frame bandpasses. Subarray observations were obtained over a six-year timeline in Cycles 17–22 and span a range of positions on the detector (e.g. the corners of all four amplifiers and the center of the both UVIS chips). These observations allow for wavelength-dependent characterization of the point-spread function (PSF) and average sensitivity for each chip, which are important for deriving the new zeropoints. They are also ideal for quantifying the accuracy of the aforementioned flat fields by comparing the observed photometry at various locations across the detector.

The encircled-energy curves were derived by Bowers et al. (2016) using observations that were reprocessed with the new chip-dependent flat fields. The full set of images was aligned for each standard star, and **AstroDrizzle** was then used to combine observations in a given filter for each UVIS chip. Cosmic-ray rejection was performed separately for short and long exposures to avoid rejecting the PSF wings in the long exposures. The number of input observations per chip ranges from two individual (e.g. narrowband imaging on UVIS 2) to 32 (e.g. broadband imaging on UVIS 1) frames.

Aperture photometry was computed at one pixel intervals for radii ranging from 1 to 75 pixels ($\sim 0''.04 - 3''.0$) with the sky determined from a 3σ -clipped mean from pixels with $r \geq 80$ pix. However the signal-to-noise was still very low for large radii ($r \geq 35 - 50$ pix, depending on the filter), and thus the encircled-energy curves are unreliable. Therefore Bowers et al. (2016) extend their encircled-energy curve using the Hartig (2009) PSFs, which were constructed from deep exposures (~ 800 s) of GD153 in two broadband filters (F275W and F625W) and interpolated over the full UVIS spectral range using an optical model. To accurately characterize the core of

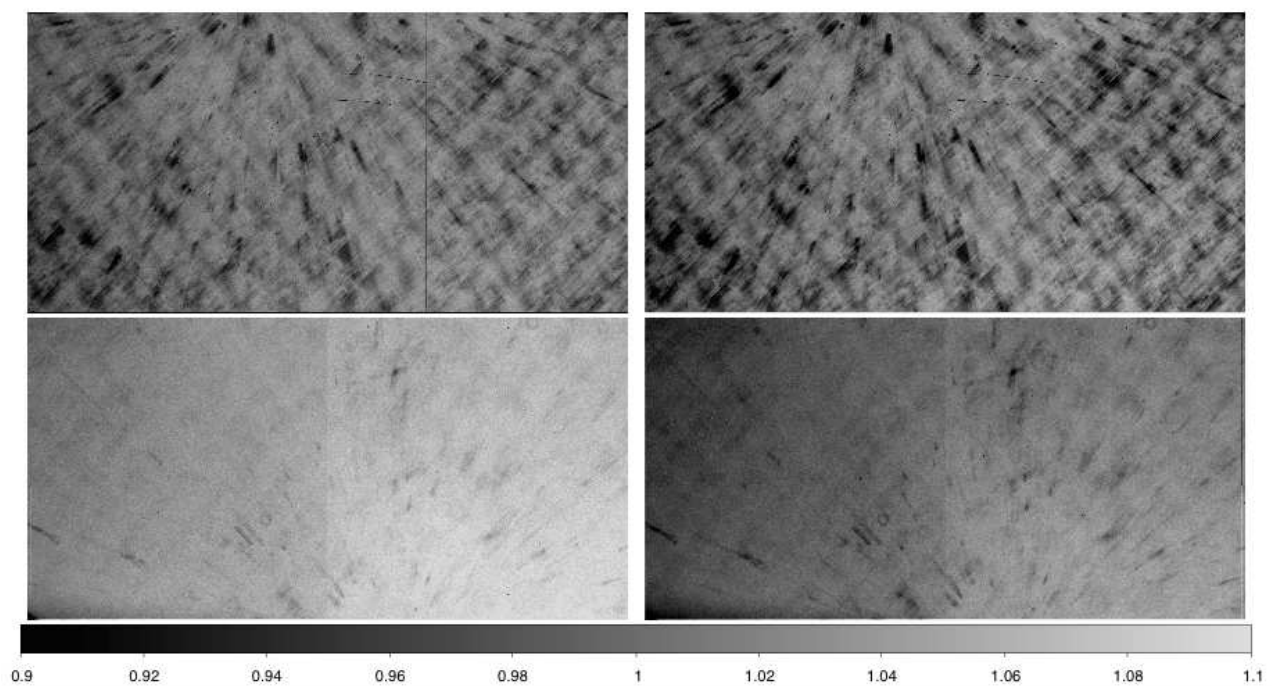


Fig. 4.— Flat-field images for F275W for 2011 (left) and 2016 (right). A key change between the two sets of flat fields is that each chip is normalized to its own median, thus accounting for their different sensitivities (ie. PHOTFLAM, see also Figure 7). The difference in quantum efficiency is reflected in different photometric zeropoints (see Deustua et al. 2016). There are similar changes to the other bandpasses as well, albeit with smaller differences for redder bandpasses. This graphic has been reproduced from Mack et al. (2016).

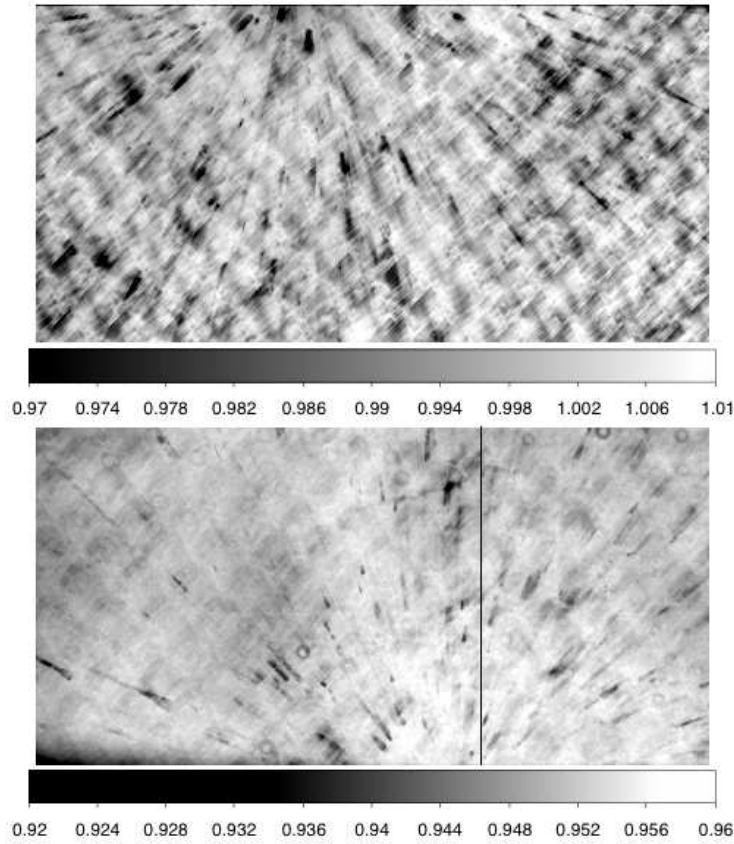


Fig. 5.— Ratio of 2011-to-2016 flat fields for F275W. It is important to note that, since the CCDs are now independently normalized to their own median values, this ratio image has a separate color scaling for each CCD. The additional medium-scale structure here is due to the correction of the sensitivity in the UV flats (obtained in ambient conditions of $-49\text{ }^{\circ}\text{C}$) to operating temperature ($-82\text{ }^{\circ}\text{C}$) as described in Mack et al. (2016) and summarized here in § 2.1. This graphic has been reproduced here from Mack et al. (2016).

the PSF without saturating (ie. $r \lesssim 2''$), Bowers et al. (2016) used the host of data with very short exposure times (1–240 s) for determining the photometric zeropoints. In Figure 6, we present the new encircled-energy curves taken from Deustua et al. (2016), which show the curves spliced together with the Hartig (2009) model.

2.3 Photometric Zeropoints

The new UVIS zeropoints are systematically $\sim 3\%$ different from the 2012 results (e.g. see our Figure 7, top panel). Deustua et al. (2016) present the revised inverse sensitivities and derived zeropoints for both CCDs. Additionally, we verified cross-instrument photometry with F775W with ACS/WFC (program ID: 9018) of 47Tuc, since the F775W filter for ACS and WFC3 are very similar in bandwidth and shape (there is only a factor of ~ 2 difference in total throughput). Furthermore both the WFC3 and ACS data were taken early in the life of each instrument, when their charge-transfer efficiencies were the highest. With these improvements to `calwf3`, the F775W photometry (corrected to an infinite aperture) between the two cameras now differs by $\sim 0.005 \pm 0.009$ mag compared to the $\sim 0.043 \pm 0.009$ mag. Based on the Pickles (1998) library of stellar spectra and the 2012 `synphot` tables, we find that the difference is $-0.025 \leq (\text{WFC3} - \text{ACS}) \leq 0.038$ mag for dwarfs earlier than M9V, and is equal to zero for $\sim \text{K7V}$ (for ST mag).

After these recalibration efforts, there are now three sets of `PHOTFLAM` (and zeropoints) values, from 2009, 2012, and 2016 (current). As noted above, the 2016 and 2012 `PHOTFLAM` values systematically differ by $\sim 3\%$ (see the top panel of Figure 7). To investigate this difference, we reanalyzed the 2012 data, which was composed of short (~ 1 s) and long (~ 10 s) exposures designed to give high signal-to-noise in the core and wings (respectively) of the standard stars. We noticed that `AstroDrizzle` systematically rejects the high signal-to-noise PSF wings as cosmic rays, and then over-weights these rejected pixels due to their longer exposure times. Consequently, the total flux of these stars is biased a few percent low, leading to the inaccurate estimates of the `PHOTFLAM` values. To avoid this effect, Bowers et al. (2016) perform cosmic-ray rejection on the short and long exposure data separately, and only combine the entire dataset once the cosmic rays have been identified. However this does not explain the similarity in the 2009 and 2012 values, since there were only short exposures available in 2009. To understand that similarity, we reprocessed the white-dwarf data for GRW+70 taken during SMOV with software and calibration files from 2009 and 2012 separately. We find that aperture photometry on amp A and C changed by $\sim 1\%$ and $\sim 2\%$, respectively. These differences amount to an average change in `PHOTFLAM` of $\sim 1\%$, which is primarily due to corrections made to the 2011 flat fields (Mack et al. 2013) to remove a large internal reflection in the 2009 ground flat-field data.

The 2016 values for `PHOTFLAM` are determined by averaging separately over each CCD with data from 2009–2015. However there are small trends in decreasing sensitivity of $\lesssim 0.1\% \text{ yr}^{-1}$ (Gosmeyer et al. 2014) and spatial variations over the detectors of $\lesssim 1\%$ (Mack et al. 2015),

particularly for the reddest bands. The WFC3 team expects to implement a time-variable zeropoint in the future to achieve $\lesssim 1\%$ photometry, though the timescale for such improvements has not been established.

2.4 New Software and Reference Files

The `calwf3` (version 3.3) software has been modified to support the new two-chip solution and CTE correction; and as part of that update, several new keywords were added to the image headers and the image-photometry table (`IMPHTTAB`) was restructured (see Table 2). The inverse-sensitivity keyword (`PHOTFLAM`) will have the same value as `PHTFLAM1` to make these changes transparent to users. We describe the many new keywords and calibration switches in Table 1. Subarrays obtained with UVIS2 will be multiplied by `PHTRATIO` to ensure sources have the same flux regardless of the chip on which they were observed.

The new `IMPHTTAB` has five extensions, listed in Table 2. Extensions 4 and 5 contain the observing mode and `PHOTFLAM` values for chip 1 (UVIS1) and chip 2 (UVIS2), respectively. The `synphot/pysynphot` tables will be updated accordingly in the Calibration Reference Data System (CRDS). Magnitudes in the ST, AB, and Vega systems are related to the inverse sensitivity (`PHOTFLAM`) by the following equations:

$$\text{STMAG} = -2.5 \log (\text{PHOTFLAM}) - \text{PHOTZPT} \quad (1)$$

$$\text{ABMAG} = -2.5 \log (\text{PHOTFLAM}) - 5 \log (\text{PHOTPLAM}) - 2.5 \log \left(\frac{10^{-8}}{c} \right) - 48.6 \quad (2)$$

$$= \text{STMAG} - 5 \log (\text{PHOTPLAM}) + 18.69 \quad (3)$$

$$\text{VEGAMAG} = \text{ABMAG} - AB_{Vega} \quad (4)$$

where $\text{PHOTZPT} = 21.10$ mag and AB_{Vega} is the AB magnitude of Vega, normalized such that $AB_{Vega} \equiv 0$ mag for the V-band.

Table 1: New Two-Chip Photometry Keywords

Keyword	Type	Description
<code>PHOTCORR</code>	string	<code>PHTRATIO</code> is computed and keywords are populated
<code>FLUXCORR</code>	string	UVIS2 is scaled to UVIS1: $\text{UVIS2} \times \text{PHTRATIO}$
<code>IMPHTTAB</code>	string	photometry-keyword reference file, defines following keywords
<code>PHTFLAM1</code>	double	inverse sensitivity for UVIS1
<code>PHTFLAM2</code>	double	inverse sensitivity for UVIS2
<code>PHTRATIO</code>	double	$\text{PHOTFLAM2}/\text{PHOTFLAM1}$

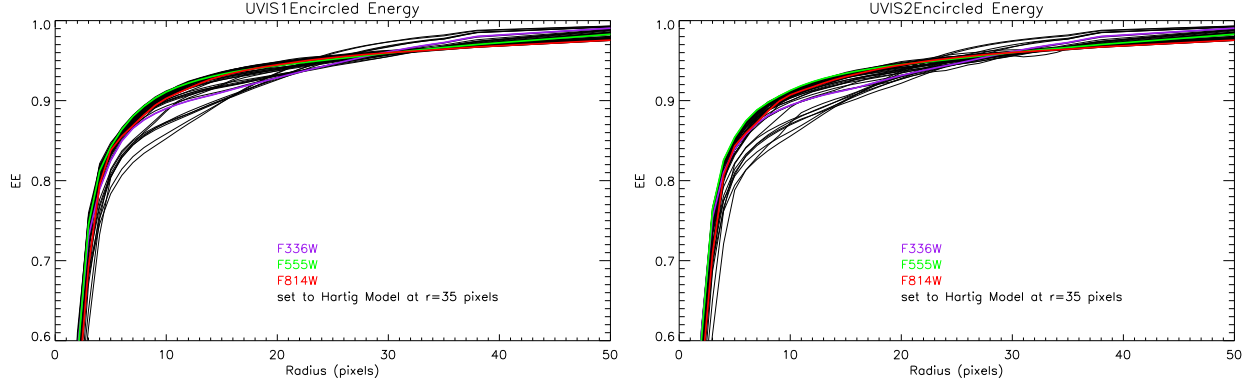


Fig. 6.— The encircled-energy curves for UVIS 1 (left) and UVIS 2 (right). Each line represents a bandpass, however we highlight three extremal bands (F336W: purple, F555W: green, and F814W: red). As described in § 2.2, Deustua et al. (2016) normalize the encircled-energy curves to the Hartig (2009) PSFs at $r=35$ pix ($1''.4$).

Table 2: Structure of IMPHTTAB

Extension	Column 1	Column 2	Column 3	Column 4	Column 5
EXT1	OBSMODE	DATA COL	PHOTFLAM	PEDIGREE	DESCRIP
EXT2	OBSMODE	DATA COL	PHOTPLAM	PEDIGREE	DESCRIP
EXT3	OBSMODE	DATA COL	PHOTBW	PEDIGREE	DESCRIP
EXT4	OBSMODE	DATA COL	PHTFLAM1	PEDIGREE	DESCRIP
EXT5	OBSMODE	DATA COL	PHTFLAM2	PEDIGREE	DESCRIP
Format	CH*40	CH*12	D(25.16g)	CH*30	CH*110

PHOTFLAM: Inverse sensitivity for UVIS1 in $\text{erg/s/cm}^2/\text{\AA}$ per e^-/s

PHOTPLAM: Filter pivot wavelength in \AA

PHOTBW: Filter bandwidth in \AA

PHTFLAM1: Inverse sensitivity for UVIS1 in $\text{erg/s/cm}^2/\text{\AA}$ per e^-/s

PHTFLAM2: Inverse sensitivity for UVIS2 in $\text{erg/s/cm}^2/\text{\AA}$ per e^-/s

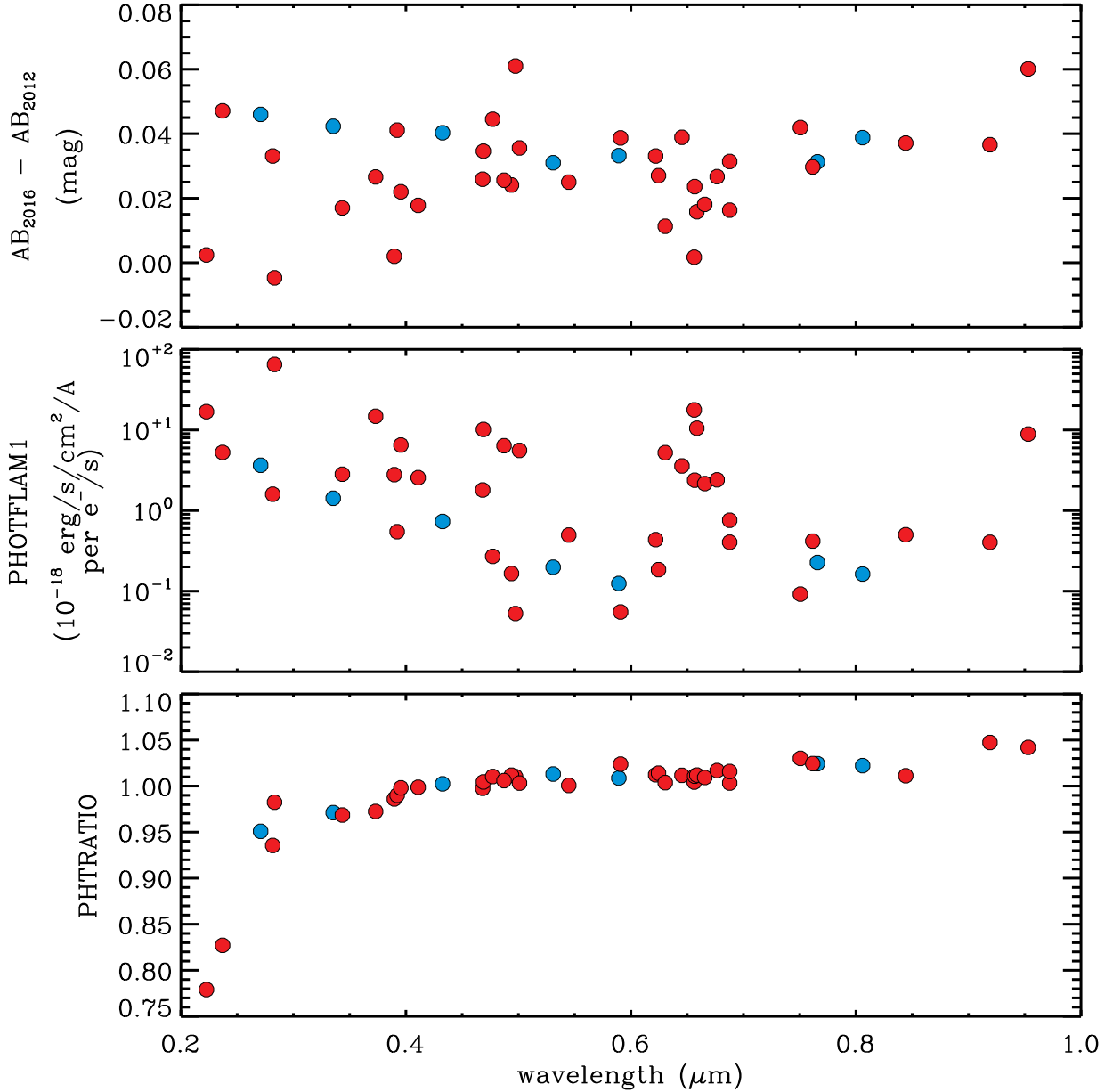


Fig. 7.— The change in the AB-zeropoints, PHOTFLAM1, and PHTRATIO as a function of wavelength for the 42 UVIS filters. The data plotted here are from Deustua et al. (2016); the blue points represent a suite of popular broadband filters (F275W, F336W, F438W, F555W, F606W, F775W, and F814W). In Equation 1, we show how the inverse sensitivity and pivot wavelength (PHOTPLAM) can be used to derive zeropoints in the ST, AB, and Vega systems (of course, the latter requires an assumed A0V stellar spectrum).

3 Charge-Transfer Efficiency Corrections

The CTE measures the reliability of a CCD to shift the charge from one pixel to the next during the readout process. A perfect detector will have a CTE of 100%, but even minute deviations from perfection ($\sim 99.9997\%$) can have profound negative consequences on image quality due to the size of modern CCD arrays. Shortly after SMOV, the effects of radiation damage became detectable, and in 2012 the WFC3 team began post-flashing the chips and developed specialized correction software. At that time, the CTE correction code was available as a stand-alone, α -distribution software modeled after the work with ACS (Anderson & Bedin 2010, Massey et al. 2010). Now with `calwf3` (version 3.3), the pixel-based CTE correction software is part of the automated calibration pipeline. *The current implementation will not correct images taken as subarrays or in binned mode (including extended-pixel edge response).*

3.1 Current WFC3/UVIS CTE Model

The WFC3/UVIS CTE algorithm fundamentally assumes that “charge traps” hold onto a number of electrons in place during the readout, while releasing them sometime later, polluting *upstream*⁴ pixels with excess charge. Although the charge traps are likely localized to certain pixels, the current model assumes traps are uniformly distributed throughout the array (Biretta & Bourque 2013; 2014; & Baggett 2014a). As of 2013, there are about ~ 500 traps per column. The current WFC3/UVIS correction algorithm incorporates the following distinct features:

1. The WFC3 algorithm works on integer numbers of electrons, and the main parameter to be calibrated is the average number of charge traps. This differs from the ACS algorithm, which permits fractional traps and defines a charge density distribution.
2. The WFC3 algorithm has additional read-noise mitigation strategies (Anderson 2013). The pixel-based CTE algorithm produces a smoothed image consistent with the observations (including the read noise and other instrumental signals).
3. The WFC3 algorithm is capable of flagging and subtracting cosmic rays that hit during the image readout. Since the full-chip readout takes ~ 90 s, a fraction of the cosmic rays (CRs) in a science image will have hit during readout; and such CRs will not undergo the same number of transfers as a CR that hit during the exposure (for the same y coordinate). Therefore in the absence of any additional measures, the trail from a readout CR will be over-subtracted. The WFC3 algorithm checks for such over-subtractions and iteratively reduces the local CTE losses until the trail is no longer negative.

⁴Here *upstream* refers to pixels that follow in the read-out process (the antonym of *downstream*).

To calibrate the WFC3 model, Anderson & Baggett (2014b) evaluated warm pixels and their trails due to CTE losses in dark-calibration images with a variety of exposure times. We briefly highlight the efficacy of the pixel-based CTE correction in § 5, but from this analysis several key points are clear:

- 1. Minimum background of 12 e⁻.** Once the effective background (ie. the sum of the bias and dark levels, astrophysical background, and instrumental postflash) reaches 12 e⁻ the 1 σ -scatter of the flux in a 3 \times 3 pix aperture is consistent with the known flux of the stars (Anderson et al. 2012; their Fig. 3). Moreover, increasing the effective background above ~ 12 e⁻ provides no additional gain in photometric quality.
- 2. Sink pixels.** As discussed in more detail below, the postflash (additional background added with an LED) effectively fills existing traps, thereby reducing source trails due to CTE losses. However it also causes sink pixels to appear as single pixels that are anomalously low in high-background images, suggesting that these are pixels with an abnormally large number of CTE traps. It is important to stress: **Sink pixels are intrinsic to the CCD chips, and for this reason, sink-pixel flagging is performed in both branches of calwf3 version 3.3 (see Figure 2).**

Based on these findings, the *de facto* standard is to postflash UVIS observations such that the total background is ~ 12 e⁻ pix⁻¹. However this standard raises the question of how to estimate the optimal postflash in preparation for an exposure. The answer requires an estimate of the effective background count rate (ie. all instrumental and/or astrophysical sources), which depends on bandpass. Baggett & Anderson (2012) tabulate the effective background fluxes for the UVIS bandpasses (see their Tab. 2). Therefore for a given bandpass, exposure time, and zodiacal background choice, it is straight-forward to compute the postflash setting:

$$\text{postflash} = \max \left(\left[12 - \mathcal{S} \times \left(\frac{t}{1000} \right), 0 \right] \right), \quad (5)$$

where \mathcal{S} is the sky flux from Baggett & Anderson (2012), t is the exposure time, and $\max(\cdot)$ is the maximum of the two values. The Exposure-Time Calculator (ETC) and Astronomer’s Proposal Tool (APT) now also account for postflash. In Table 3, we describe the host of new keywords in UVIS headers that control aspects of the CTE correction.

3.2 Reasons to OMIT the CTE Corrections

For most science applications, users will prefer CTE-corrected images. However the WFC3/UVIS algorithm described above is a statistical correction to the pixel values, and we can foresee at least three reasons a user might wish to work with the CTE-*uncorrected* data (ie. FLT or DRZ files).

1. Every attempt has been made to build an algorithm capable of identifying and correcting cosmic rays that hit during readout. However these pixels are very challenging to correct, and the algorithm is known to “over-correct” in many cases. Over-corrected, readout cosmic rays will have a series of negative upstream pixels that asymptotically approach zero.
2. The pixel-based CTE correction⁵ is, by the very nature of the problem, incapable of a perfect correction, due to the presence of read noise. Since we have no measure of the *true* number of electrons in a given pixel, the algorithm will weakly amplify the noise (Anderson & Bedin 2010). For many applications, this is negligible; however some users might prefer a method that does not amplify noise. In general, such an algorithm would require assumptions on the intrinsic flux of a source and therefore require some type of “forward model” for CTE. Similarly a “catalog-based” approach, where the aperture photometry is corrected based on the y -position in the detector, can perform well, but is only valid for point sources (Noeske et al. 2012; Baggett, Gosmeyer, & Noeske 2015). At present, `calwf3` (version 3.3) does not provide any mechanism for such a correction, since it entails all the subtleties of source identification and classification.
3. The current correction algorithm has only been tested on nearly blank fields, such as star fields or deep fields. While we expect the algorithm to perform *better* on images with extended objects (such as large nebulosities or extended galaxies) due to self shielding of the charge⁶, we have not yet tested this regime. This point is less concerning than the previous two, but it may be important for certain use cases.

4 Sink Pixels

With the advent of postflashing in 2012, a new type of image defect was identified (see Biretta & Bourque (2014) for the discovery and Anderson & Baggett (2014a) for a more thorough analysis). These pixels contain a modest number of charge traps (typically 20–100 e^-), and thus when read out, do not correctly report the number of electrons generated in these pixels. Sink pixels simply have lower counts than adjacent “normal” pixels (see Figure 4 of Anderson & Baggett 2014b). This phenomenon is distinct from normal pixel-to-pixel sensitivity, in that photons that interact with sink pixels *do* generate electrons, but some of these electrons do not shuffle out of the pixel during readout, and are thus not recorded with the pixel. In short, *this effect has been found to be additive, not multiplicative*. Investigations suggest that sink pixels are created by cosmic ray events (Anderson & Baggett 2014a; 2014b); thus it appears that most of

⁵http://www.stsci.edu/hst/wfc3/tools/cte_tools

⁶Self-shielding is the process whereby electrons on the leading edge of a large object fill the traps, and upstream pixels are then less affected — effectively increasing the sky background for upstream pixels. Therefore the fractional error in the photometry is expected to be small.

the sink pixels may be a consequence of on-orbit radiation damage.⁷ At present, no sink pixel has been found to heal or be recovered.

The impact of sink pixels on the background level depends on their locations in an image. For images with high backgrounds ($\sim 85 \text{ e}^-$) and for sink pixels near the readout register, the sink pixels have little effect on upstream pixels in the same column. However, for lower backgrounds (as is typical for many science exposures) or far from the readout register, the sink pixels can have profiles that extend $\lesssim 10 \text{ pix}$ *upstream*, reflecting the fact that it takes several pixels of background to “fill” the traps in the sink pixel. In Figure 8 (taken from Anderson & Baggett 2014a), we see that a single sink pixel can affect both downstream pixels and several upstream pixels, depending on the background. So although sink pixels are rare ($\sim 0.05\%$ of the detector), in low-background imaging they can corrupt as much as $\sim 0.5\%$ of the detector.

Since the behavior of the sink pixels is scene-dependent, the WFC3 team has decided to take a conservative approach to flag all pixels in a given image that are likely to be affected. In the event that a bright source lands on a sink pixel (or even the streak of a sink pixel), the effective background experienced by the pixel will be higher than the neighboring regions. As described above, the behavior of this particular sink pixel or streak is now altered with respect to other sink pixels. By analyzing a host of RAW bias images with varying levels of postflash, Anderson & Baggett (2014b) identified 41,762 sink pixels that produce streaks that affect $\sim 6 \times 10^5$ pixels. From this they generated a new reference file: **SNKCFIL**E that contains the modified-Julian date (MJD) of the appearance of the sink pixel on orbit. The new **calwf3** (version 3.3) uses the **SNKCFIL**E by populating the data-quality array of a science image with 1024 for flagged pixels in the following multi-stage fashion:

1. If **SNKCFIL**E value is $> 100\,000$ (recalling that the units are MJD), then **calwf3** (version 3.3) performs a date check. If $\text{MJD}(\text{SNKCFIL}) < \text{MJD}(\text{science image})$, then flag the science pixel.
2. If a pixel is flagged as a sink pixel *AND* its downstream pixel in the **SNKCFIL**E is -1 , then flag the downstream pixel.
3. While moving along the sink-pixel trail, if a sink pixel has been flagged *AND* the **SNKCFIL**E value of an upstream pixel is greater than the value of the sink pixel in the science image, then flag the upstream pixel. Continue flagging trail pixels until either (a) the **SNKCFIL**E upstream pixel value is 0 or (b) the **SNKCFIL**E upstream pixel value is less than the value of the sink pixel in the science image.

All pixels flagged as sink pixels (or affected by a sink-pixel trail) are not used during any processing steps within **calwf3**. We schematically illustrate this file in Figure 9.

⁷Only a very small population of sink pixels were found in data taken before launch (Anderson & Baggett 2014b).

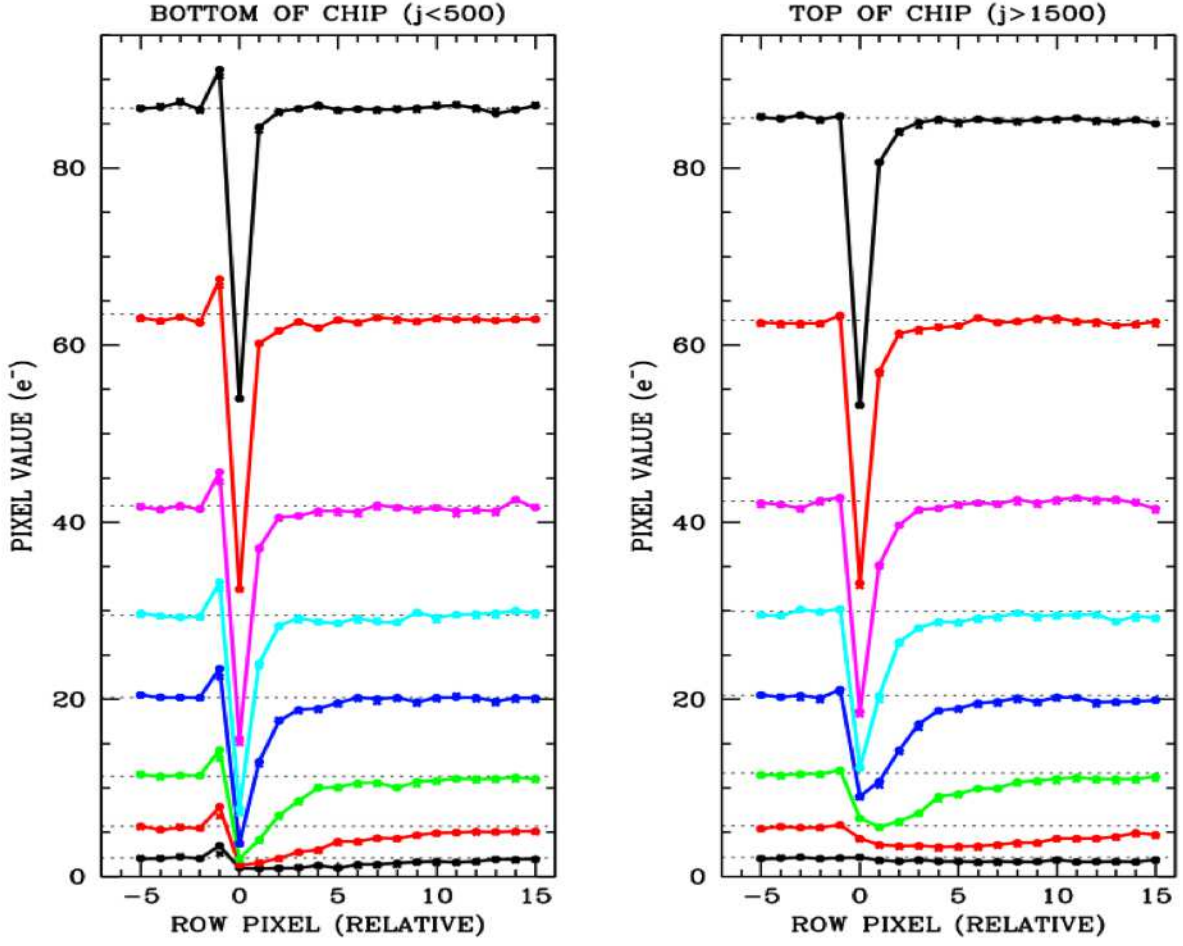


Fig. 8.— The average profiles of sink pixels with 35 traps. This graphic is reproduced here from Anderson & Baggett (2014a, their Fig. 3). The colors represent various background levels, with 2, 5, 10, 20, 30, 40, 65, and 85 e^- from the bottom to the top. The left and right panels show the average profile for sink pixels near the bottom (near the readout register) and top (far from the readout register), respectively. The increased number of transfers for the sink pixels near the top (right panel) causes more flux to be lost, which effectively blurs the profile by charge-transfer inefficiency. Roughly 20 – 30% of the time, the pixel *immediately preceding* the sink pixel (ie. $\Delta y = -1$) in the readout appears high. The cause for this behavior is not yet known, but it is suspected to be caused by the readout itself during the charge-shuffling stage.

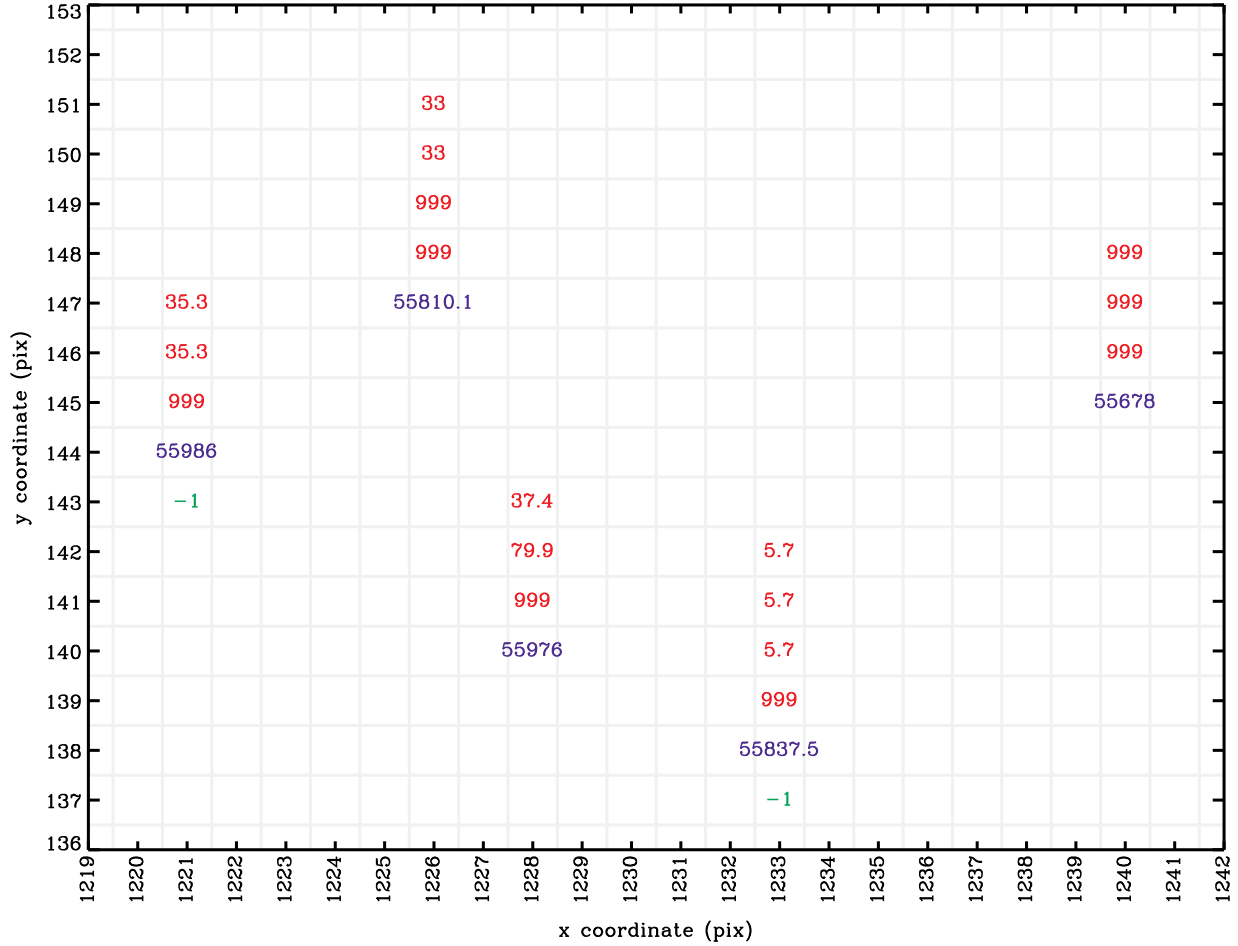


Fig. 9.— Schematic of the sink-pixel file. We show the sink (blue), enhanced downstream (green), and low upstream (red) pixels. Empty pixels have zero and are not impacted by sink pixels. The sink pixels (blue values) are the MJD of the appearance of the sink pixel, whereas other values (green and red) are the excess flux (lost and removed, respectively) from that sink pixel. The new `calwf3` will *only* flag bad pixels with 1024 in the data-quality arrays if the exposure was taken *after* the appearance of a given sink pixel. Presently no corrections to the science images are made nor is it clear that sink pixels can be “healed” or recovered over time. This graphic was adapted from Baggett et al. (2014).

5 Validation

5.1 Photometry and Astrometry

We tested the effects of the UVIS pixel-based CTE corrections by comparing photometry and astrometry of stars in the cluster NGC 2203 (PropID: 12257), which is similar to that described in Kozhurini-Platais et al. (2007) for ACS. These UVIS data were taken in F336W, F475W, and F814W in short, intermediate, and long exposures with the small-scale dither pattern and no postflash. We determined the flux and (x, y) -positions for each star on individual exposures using the PSF-fitting techniques (Anderson & King 2006; Kozhurina-Platais, Goudfrooij, & Puzia 2007).

To compare photometry and astrometry before and after the CTE corrections, we used short (120 s) and long (700 s) exposures in F475W. We selected the set of stars common to both images by linearly transforming the (x, y) -positions from the short to the long exposures with a matching tolerance of 0.1 (native) pixels. In Figure 10, we show the differences in brightness and y -position for no-CTE correction (left) and CTE correction (right). It is clear that in the absence of a CTE correction, undesirable effects are imprinted on several basic measurements.

5.2 Color-Magnitude Diagram

Using the data described in § 5.1, we demonstrate that photometry processed with the improved UVIS pipeline and CTE correction does not change the inferred astrophysical properties of NGC 2203. Early photometric results are based on data reduction with no CTE corrections and photometric calibrations derived right after SMOV (Goudfrooij et al. 2014). Here we present color-magnitude diagram (CMD) for selected stars inside the cluster core radius (Goudfrooij et al. 2014), derived from the photometry with CTE-corrected images, new L-flats, and new photometric calibrations. To obtain the cluster age, distance, and differential reddening we used Padova evolutionary isochrones for different ages (0.83 Gyr with steps of 0.1 Gyr) and stellar metallicities (0.006, 0.008, and 0.01). In Figure 11, we show the CMD with the best-fitting isochrones (red lines) of different ages. The parameters of the fitted isochrones (such as age, distance modulus, and reddening) are consistent with those found by Goudfrooij et al. (2014). The derived observational CMD closely follow all stages of the theoretical stellar isochrones: from the faint stars on the main sequence through the turnoff point, sub-giant branch, red-giant branch, and red-giant clump.

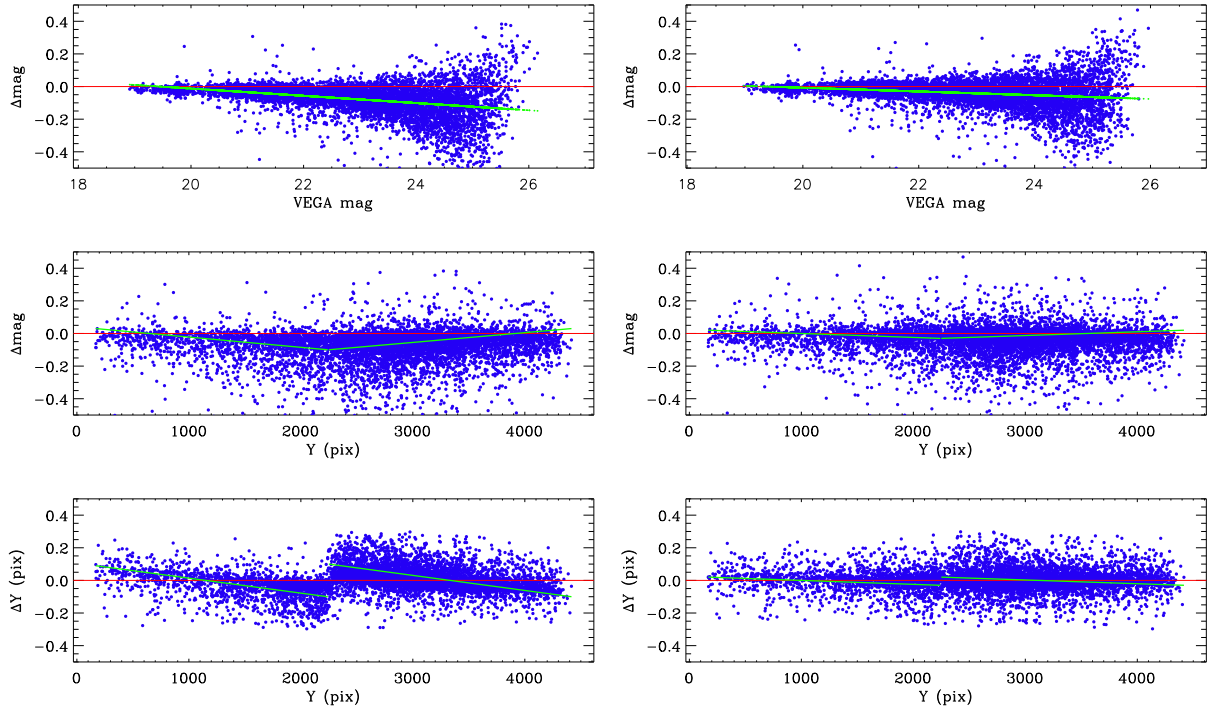


Fig. 10.— Differences in brightness and y -position between short and long exposures for NGC 2203 without CTE-correction (left) and CTE-correction (right). The brightness for faint stars (~ 25 mag) is off by ~ 0.2 mag without the CTE correction, which is reduced to $\lesssim 0.05$ mag after the correction (compare top rows). The middle rows show the same brightness difference as a function of y -position — the discontinuity at $y = 2048$ arises from the different readout directions for the two chips. The bottom row shows the difference in y -position as function of y , and that the CTE correction clearly removes a major systematic in the observed positions.

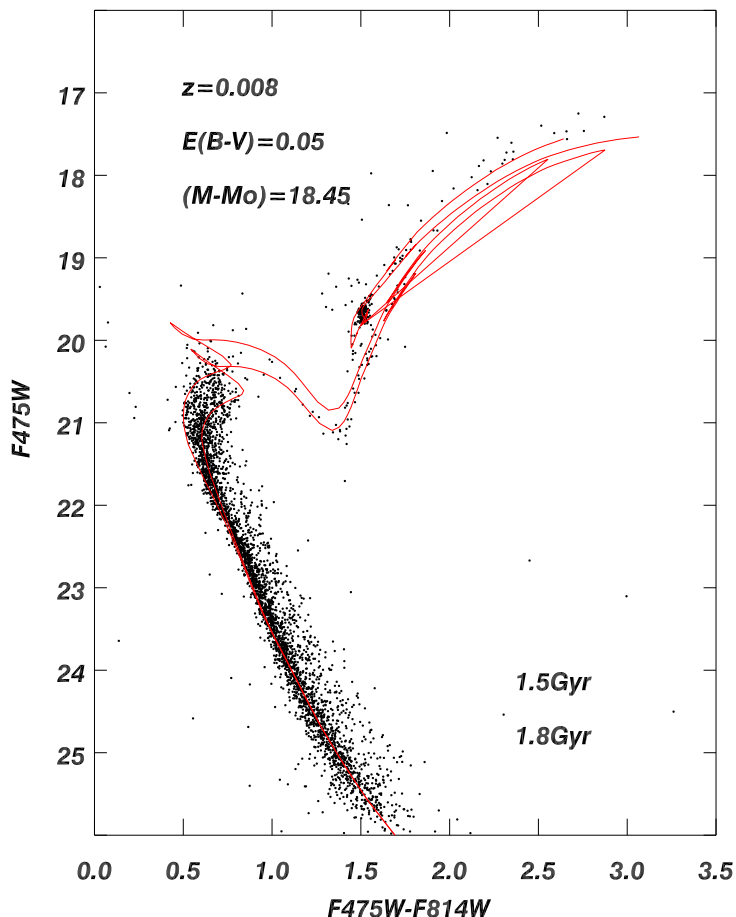


Fig. 11.— CMD for NGC2203. Here we only show stars within the published core radius (Goudfrooij et al. 2014) and in red overplot the best fitting isochrone. In the legends we give the best-fitting values for the stellar metallicity, color excess, distance modulus, and stellar population ages.

6 Additional Minor Revisions in calwf3 (version 3.3)

6.1 Improved UVIS Dark Calibration

The new version of `calwf3` (version 3.3) utilizes an updated dark-reference file with three key improvements over previous versions and is discussed by Biretta & Bourque (2014). We illustrate the new algorithm in Figure 12, and full details will be presented in a forthcoming ISR (Bourque

& Baggett 2016). Improved dark-reference files have been generated for all on-orbit data and are accessible by retrieving science data from the MAST archive, or by manual offline reprocessing using the products found in the CRDS.

6.1.1 CTE-corrected reference files

To support the generation of CTE-corrected data products (eg. FLC, DRC) in the pipeline, we provide CTE-corrected dark calibration-reference files (ie. DKC). The reference files are now constructed from individual CTE-corrected UVIS darks (ie. RAC files) instead of uncorrected data (ie. RAW files). The CTE correction helps to mitigate background signal introduced by CTE losses from hot pixels and cosmic rays that are commonly found in dark observations (see Figure 13). Note that uncorrected dark calibration-reference files (ie. DRK) continue to be provided and used by `calwf3` (version 3.3) for calibration of standard data products (ie. FLT files).

6.1.2 Improved temporal accuracy of hot pixel populations

The UVIS hot pixel population (defined as pixels that have a dark current exceeding $54\text{ e}^- \text{ hr}^{-1}$ and marked with a bit value of 16 in the data-quality array) is constantly evolving on both long and short-term timescales. With roughly 1000 new hot pixels appearing each day, and a monthly anneal procedure that currently mitigates 20–30% of the population, some hot pixels are permanent while others are only temporary. Prior to this release, dark reference files were generated on a hard four-day cadence in order to accurately measure the hot pixel population for a given UVIS observation. As a consequence, science observations that happen to occur towards the beginning or end of this four-day window would have too many or too few hot pixels flagged, respectively. Now reference files on a daily cadence, or a running four-day window, resulting in an even more accurate flagging of the hot pixel population.

6.1.3 Improved accuracy of dark current measurement

In the previous algorithm, all non-hot pixels (i.e. those that have a dark current below $54\text{ e}^- \text{ hr}^{-1}$) in the dark reference files were set to the median value of the frame, resulting in a uniform dark current rate for the vast majority of pixels and the averaging over any spatial variations in the dark current. In the new algorithm, non-hot pixels are set to a “masterdark” value that is computed by averaging all individual dark observations from the appropriate anneal cycle (i.e. all darks observations occurring between two UVIS anneal procedures, nominally ~ 100 observations), which provides an accurate dark current measurement for each individual pixel. Figure 14 shows the resulting pixel values in an example UVIS dark using the previous algorithm and the new algorithm.

Table 3: New CTE Keywords

Keyword	Type	Description
PCTECORR	string	CTE corection switch
PCTETAB	string	CTE correction table (sets CTE correction parameters below)
DRKCFILE	string	detrailled dark reference file
BIACFILE	string	average bias from in CTE correction
SNKCFILE	string	map of sink pixels
CTE_NAME	string	name of CTE algorithm
CTE_VER	string	version of the CTE algorithm
CTEDATE0	double	MJD of UVIS installation on HST
CTEDATE1	double	MJD of CTE model pinning
PCTETLEN	integer	maximum length of CTE trail
PCTERNOI	double	read noise (in e^-)
PCTENFOR	integer	number of iterations in CTE forward modeling
PCTENPAR	integer	number of iterations in parallel transfer
PCTEFRAC	double	scaling of CTE model relative to CTEDATE1
PCTENSMD	integer	read noise mitigation algorithm
PCTETRSH	float	over-subtraction threshold for readout CRs

For more detail on these keywords, see Baggett et al. (2014).

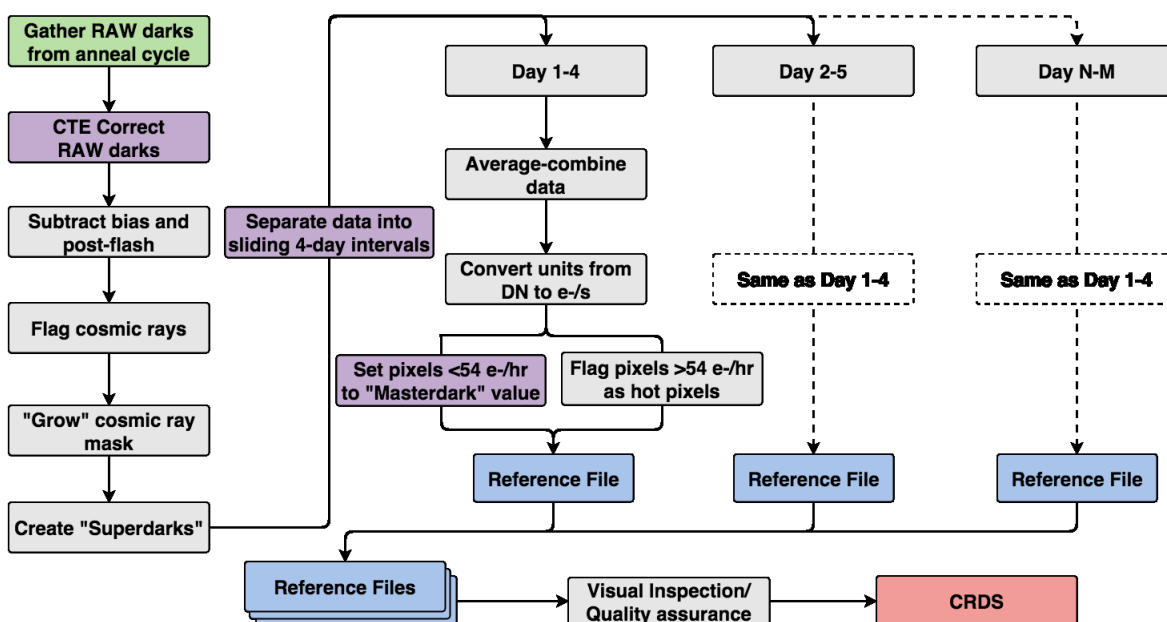


Fig. 12.— A flow chart showing the nominal dark-reference file generation algorithm as well as the three new features implemented in the `calwf3` (version 3.3 — magenta boxes).

6.2 Channel-Select Mechanism

WFC3 is able to switch between the UVIS and IR channels by means of a channel-select mechanism (CSM), where the CSM is *in the beam* for IR and *out of the beam* for UVIS. In the primary extension of both UVIS and IR data, we now include the `CSMID` keyword (formerly available only in the SPT engineering files).

6.3 Scanning-Mode for IR Data

While not directly relevant for UVIS, we briefly highlight two minor changes to the fits headers and IR image processing for completeness. First, all the scan-related keywords (see Table 4), formerly accessible only via the engineering file headers (SPT files), will now be present in the calibrated science data headers (ie. FLT/FLC files). Second, the default for the cosmic-ray correction calibration step (keyword `CRCORR`) is now `OMIT`, disabling the up-the-ramp fitting in `calwf3` (version 3.3). In some cases of time-varying background levels, the up-the-ramp fitting in `calwf3` leads to significant errors in the final products (Brammer et al. 2014). The simplest approach is to generate science data (FLT files) from the multiaccum readout with the *last-minus-first*, which is simply the average count rate determined by differencing last and first reads. The last-minus-first approach cannot flag cosmic rays or reduce the read noise like the classic up-the-ramp fitting, but provides a better estimate of the sky brightness distribution (e.g. Brammer et al. 2014). Observers with existing scan data may retrieve their files from the MAST archive to obtain the improved products.

7 Summary

The switch to the updated `calwf3` (version 3.3) should require not any changes to existing pipelines for users, but will vastly enhance the quality of final data products. All WFC3/UVIS data requested through MAST after Feb. 23, 2016 will be processed by the `calwf3` (version 3.3). In summary, there are several key features:

Two-Chip Photometry: The new standard for processing WFC3/UVIS data is to decouple the calibrations for the two CCDs. No there are completely independent calibrations and reference files for improved performance, especially when combining observations from different detectors with `AstroDrizzle`.

Charge-Transfer Efficiency Corrections: Prior to the release of `calwf3` (version 3.3), the corrections for the loss in charge-transfer efficiency were only performed by users with stand-alone code. These corrections have now been fully integrated within `calwf3` (version 3.3). However the uncorrected data are still produced and available through MAST.

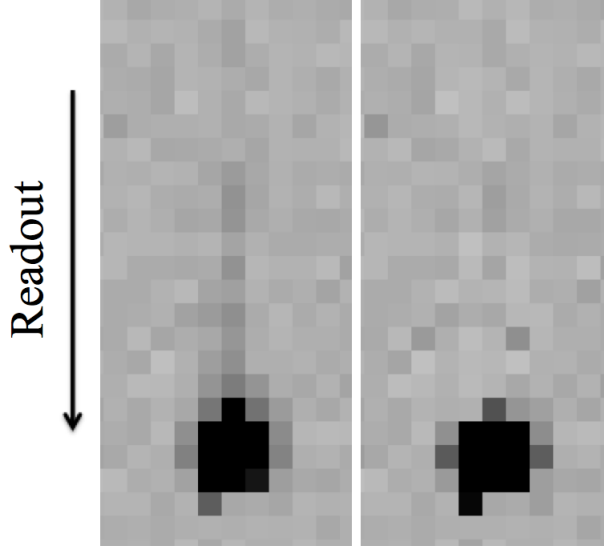


Fig. 13.— An example of a cosmic ray in a nominal $12\ e^-$ postflashed 900 s UVIS dark (left) and a postflashed and CTE-corrected dark (right), showing the benefit that the CTE correction has on signal trails caused by CTE losses.

Table 4: Scan Keywords[†]

Keyword	Type	Description
SCAN_TYP	string	C:bostrophidon; D:C with dwell; N:N/A
SCAN_WID	double	scan width (arcsec)
ANG_SIDE	double	angle between sides of parallelogram (deg)
DWELL_LN	integer	dwell pts/line for scan pointing (1-99,0 if NA)
DWELL_TM	double	wait time (duration) at each dwell point (sec)
SCAN_ANG	double	position angle of scan line (deg)
SCAN_RAT	double	commanded rate of the line scan (arcsec/sec)
NO_LINES	integer	number of lines per scan (1-99,0 if NA)
SCAN_LEN	double	scan length (arcsec)
SCAN_COR	string	scan coordinate frame of ref: celestial,vehicle

[†]Formerly only accessible in the SPT files.

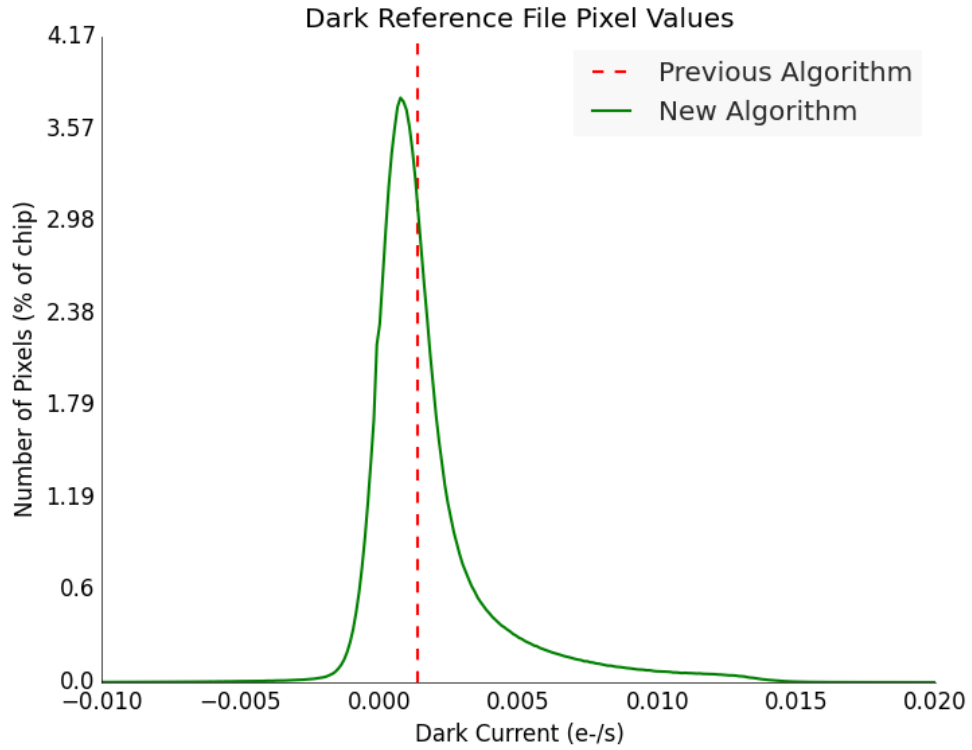


Fig. 14.— A histogram showing the pixel values in an example UVIS dark reference file generated using the previous algorithm (red) and the new algorithm (green). Note that the new algorithm values exhibit a normal distribution, whereas the previous algorithm employed a flat median value.

Sink Pixels: As postflash was becoming the *de facto* standard for mitigating the problems with CTE, a new type of image defect was discovered. The WFC3 team has developed a new calibration reference file to mask sink pixels and their associated trails.

There are several minor improvements concerning the productions of the dark reference files and header keywords. For more details on any of these features, we refer users to the individual ISRs from which this Reference Guide was prepared.

8 Acknowledgments

Our thoughts and fondest memories remain with T. Dahlen, a dedicated member of the WFC3 team and the HST community. We are very grateful to M. Fall for the thorough review and excellent comments that had a significant impact on the quality of this report.

9 References

- Anderson, J. *Instructions for Using the Alpha-Release of the WFC3/UVIS Pixel-based CTE Correction*, http://www.stsci.edu/hst/wfc3/tools/cte_tools/wfc3cte_alpha.docx, white paper
- Anderson, J. & Baggett, S. *Sink Pixels and the CTE in the WFC3/UVIS Detector*, WFC3 ISR, 2014a-19
- Anderson, J. & Baggett, S. *Flagging the Sink Pixels in WFC3/UVIS*, WFC3 ISR 2014b-22
- Anderson, J. et al. *The Efficacy of Post-Flashing for Mitigating CTE-Losses in WFC3/UVIS Images* 2012, white paper
- Anderson, J. & Bedin, L. R. *An Empirical Pixel-Based Correction for Imperfect CTE. I. HST's Advanced Camera for Surveys* 2010, PASP, 122, 1035
- Anderson J., King, I., 2006, *PSFs, Photometry, and Astrometry for the ACS/WFC ACS* ISR-2006-01
- Baggett, S. & Anderson, J. 2012, *WFC3/UVIS Sky Backgrounds* WFC3 ISR, 2012-12
- Baggett, S., Anderson, J., & Sosey, M. 2014, *WFC3/UVIS CTE Correction: Requirements for new keywords and reference files*, WFC3 TIR 2014-03
- Baggett, S., Gosmeyer, C., & Noeske, K. 2015, *WFC3/UVIS Charge-Transfer Efficiency 2009–2015* WFC3, ISR 2015-03
- Bajaj, V., *The Updated Calibration Pipeline for WFC3/UVIS: A Cookbook to UVIS2.0*, WFC3 ISR-2016-02
- Biretta, J. & Bourque, M. *WFC3 Post-Flash Calibration*, WFC3 ISR 2013-12
- Biretta, J. and Bourque, M., *WFC3 Cycle 19 & 20 Dark Calibration: Part I* WFC3 ISR 2014-04.
- Bourque, M. & Baggett, S. *UVIS2.0 Dark Calibration: Improved Algorithm and Monitoring Results*, WFC3 ISR-2016-08
- Bowers, A., Mack, J., Deustua, S. *UVIS2.0: Encircled Energy*, WFC3 ISR-2016-04
- Brammer, G. *Time-varying Excess Earth-glow Backgrounds in the WFC3/IR Channel*, WFC3 ISR 2014-03
- Deustua, S., Mack, J., Bowers, A. et al. *UVIS2.0: Photometric Calibration*, WFC3 ISR-2016-03
- Deustua, S., et al. *UVIS2.0: Synphot/PySynphot File Updates*, WFC3 ISR-2016-07
- Dressel, L., 2015, “Wide-Field Camera 3 Instrument Handbook, Version 7.0”
- Giavalisco, M. *Minimizing CTE Losses in the WFC3 CCDs: Post Flash vs. Charge Injection*, WFC3 ISR 2003-01
- Gosmeyer, C. M., et al. *Update on the WFC3/UVIS Stability and Contamination Monitor* WFC3 ISR 2014-20
- Goudfrooij, P., et al. *Extended Main-Sequence Turnoffs in Intermediate-age Star Clusters: A Correlation between Turnoff Width and Early Escape Velocity* 2014, ApJ, 797, 35
- Hartig, G. *WFC3 SMOV Programs 11436/8: UVIS On-orbit PSF Evaluation*, WFC3 ISR 2009-38
- Kozhurina-Platais, V., Goudfrooij, P., & Puzia, T. 2007, *ACS/WFC: Differential CTE Correction for Photometry and Astrometry from non-Drizzled Images* ACS ISR-2007-04
- Mack, J., Sabbi, E., & Dahlen, T. *In-flight Corrections to the WFC3 UVIS Flat Fields*, WFC3 ISR 2013-10

- Mack, J., Rajan, A., & Bowers, A. *Spatial Accuracy of the UVIS Flat Fields* WFC3 ISR 2015-18
- Mack, J., Dahlen, T., Sabbi, E., & Bowers, A. 2016 *UVIS2.0: Chip-Dependent Flats* WFC3 ISR-2016-04
- Mack, J. 2016 *UVIS 2.0: Ultraviolet Flats* WFC3 ISR 2016-05
- Massey, R. *Charge transfer inefficiency in the Hubble Space Telescope since Servicing Mission 4* 2010, MNRAS, 409, L109
- Noeske, K., Baggett, S., Bushouse, H., Petro, L., Gilliland, R., Khozurina-Platais, V. *WFC3 UVIS Charge Transfer Efficiency October 2009 to October 2011* WFC3 ISR 2012-09
- Pickles, A. J., 1998, PASP, 110, 863